



OPEN

Regionally-triggered geomagnetic reversals

Filipe Terra-Nova  & Hagay Amit

Systematic studies of numerical dynamo simulations reveal that the transition from dipole-dominated non-reversing fields to models that exhibit reversals occurs when inertial effects become strong enough. However, the inertial force is expected to play a secondary role in the force balance in Earth's outer core. Here we show that reversals in numerical dynamo models with heterogeneous outer boundary heat flux inferred from lower mantle seismic anomalies appear when the amplitude of heat flux heterogeneity is increased. The reversals are triggered at regions of large heat flux in which strong small-scale inertial forces are produced, while elsewhere inertial forces are substantially smaller. When the amplitude of heat flux heterogeneity is further increased so that in some regions sub-adiabatic conditions are reached, regional skin effects suppress small-scale magnetic fields and the tendency to reverse decreases. Our results reconcile the need for inertia for reversals with the theoretical expectation that the inertial force remains secondary in the force balance. Moreover, our results highlight a non-trivial non-monotonic behavior of the geodynamo in response to changes in the amplitude of the core-mantle boundary heat flux heterogeneity.


In order to simulate magnetic field reversals using self-consistent 3D simulations of core convection in a spherical shell^{1,2}, the convection should be sufficiently vigorous³. However, under such conditions inertial effects become significant^{4–6} hence the fluid dynamics might depart from an Earth-like force balance. Earth's core dynamics are governed by a zeroth-order quasi-geostrophic balance, with the ageostrophic Coriolis force expected to be balanced by Archimedes and Lorentz forces (termed QG-MAC, see^{7–12}). It therefore remains a challenge to simulate reversals while maintaining an Earth-like force balance with secondary inertial effects.

The above mentioned systematic parametric studies of numerical dynamos were performed using homogeneous boundary conditions. However, heterogeneous boundary conditions have often been invoked in numerical dynamos to recover various observations related to the geomagnetic field, its secular variation and the core convection that generates it (e.g.^{13–23}). Over much longer timescales, mantle control on the geodynamo was also proposed to explain the strongly time-dependent paleomagnetic reversal frequency (e.g.^{24–27}).

Here we show that the impact of lower mantle heterogeneity on the geodynamo may reconcile the existence of reversals and an Earth-like force balance. We start from a dynamo model with homogeneous boundary conditions in the well-established, dipole-dominated non-reversing regime. Then we impose a heterogeneous outer boundary heat flux inferred from a lower mantle tomography model (Fig. SM1;²⁸) and we gradually increase the amplitude of the heat flux heterogeneity q^* (see Methods and Table SM1).

Results

Figure 1 compares two dynamo models, one with a relatively low amplitude of heat flux heterogeneity (Figs. 1a,c) vs. another with a larger q^* value (Figs. 1b,d). In the case of a relatively weak boundary heterogeneity, the ratio of magnetic to kinetic energies in the shell [which is considered as a proxy to reversals, see¹¹] is larger than unity and the field never reverses (Fig. 1a). At the top of the shell, the inertial force is significantly smaller than the dominant first order ageostrophic Coriolis force (Fig. 1c), as expected for a QG-MAC force balance⁸. In contrast, in the case of a stronger boundary heterogeneity, the ratio of magnetic to kinetic energies in the shell is lower including some periods in which it dips below unity, and the field exhibits reversals (Fig. 1b). Overall the inertial force is still significantly weaker than the ageostrophic Coriolis force - note that the peak of the former is four times smaller than the peak of the latter (see scale difference in Fig. 1d). In our dynamo models the ageostrophic Coriolis force in the two horizontal directions is indeed mostly balanced by the Lorentz force (see Fig. SM2). However, some localized inertial force signatures appear, especially below regions of large outer boundary heat flux (see dashed contours in Fig. 1d). In this snapshot strong localized inertial force features are concentrated mostly below the Americas, though at other snapshots these structures alternate between the Americas and east Asia, the two regions where the imposed outer boundary heat flux is large. Away from these narrow stripes, the

Nantes Université, Univ Angers, Le Mans Université, CNRS, Laboratoire de Planétologie et Géosciences, LPG UMR 6112, 44000 Nantes, France.  email: filipe.terranoval@univ-nantes.fr

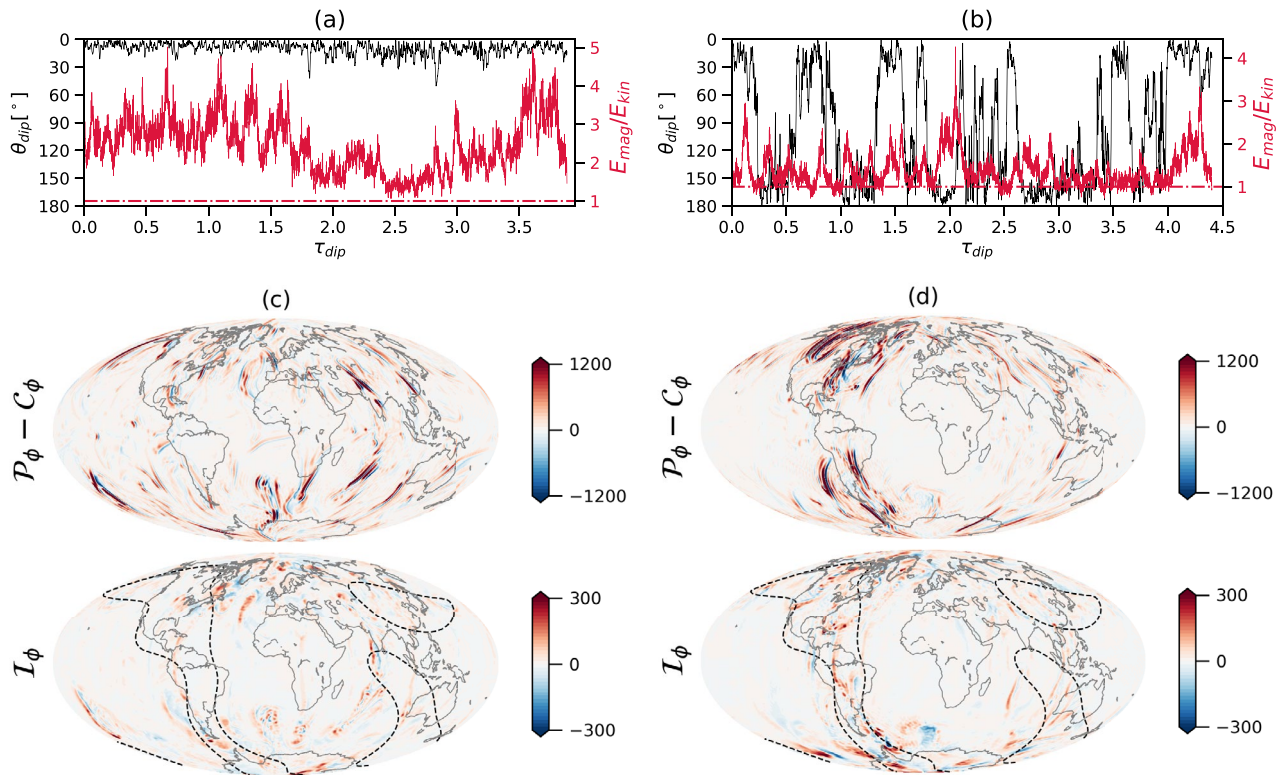


Figure 1. The distance of the dipole axis from the north geographic pole (black) and the ratio between magnetic energy and kinetic energy (red) vs. time in units of dipole diffusion times for two numerical dynamo simulations. In both cases the Ekman number is $E = 1 \times 10^{-4}$, the Rayleigh number is $Ra = 4 \times 10^7$, the Prandtl number is $Pr = 1$ and the magnetic Prandtl number is $Pm = 8$ (for definitions of the non-dimensional numbers see Methods). The amplitude of the imposed outer boundary heat flux heterogeneity (see Fig. SM1) is $q^* = 0.4$ (a) and $q^* = 1.0$ (b). Red point-dashed lines denote $E_{mag}/E_{kin} = 1.0$. The non-dimensional azimuthal components of the ageostrophic Coriolis and Inertia forces $\mathcal{P}_\phi - \mathcal{C}_\phi$ and \mathcal{I}_ϕ at the top of the shell (radial level $r/r_o = 0.95$ where r_o is the core radius) for a typical snapshot of the model with $q^* = 0.4$ are shown in (c), and the same forces for the model with $q^* = 1.0$ are shown in (d). Note the different scales of the energy ratios in (a) vs. (b) and the different scales in ageostrophic Coriolis vs. inertia forces in (c,d). Dashed black contours denote half maximum of the imposed outer boundary heat flux anomaly in (c,d).

inertial force is much weaker. Volumetric averages of the forces in our dynamo models (Fig. SM3) confirm the dominance of quasi-geostrophy, with the residual ageostrophic Coriolis force balanced by the buoyancy force at large scales and the Lorentz force at small scales (i.e. QG-MAC¹¹). The inertial force is an order of magnitude smaller than the ageostrophic Coriolis force (Fig. SM3).

Figure 2 summarizes some key diagnostics for all the dynamo models, which reveal the dependence of the reversibility on the amplitude of heat flux heterogeneity q^* . Increasing effects of mantle control from the homogeneous case up to $q^* = 1.0$ increases the tendency of the dynamo models to reverse, as evident by the increase in the local Rossby number (black) and decrease in the dipolarity of the field (symbol size) (Fig. 2) that result in the increase in the time-average dipole tilt (Fig. SM4), in agreement with most previous studies (e.g.^{6,25}). However, further increase in q^* causes, somewhat surprisingly, opposite trends in these diagnostics, i.e. a decrease in the reversibility (Figs. 2 and SM4).

These two opposite trends can be explained in terms of our regional measures of mantle control (see Methods). For moderate mantle control ($q^* < 1$), increasing q^* leads to stronger inertial force at regions of large outer boundary heat flux (red dashed contours in Fig. SM1, red in Fig. 2), i.e. the reversals are triggered regionally by inertial effects, while globally inertia is far too weak to play a role in the first order force balance. The impact of the core-mantle boundary (CMB) heat flux heterogeneity is also visible in the morphology of the radial magnetic field on the outer boundary during a reversal (Fig. 3). Before (Fig. 3a) and after (Fig. 3d) the reversal, intense high-latitude normal polarity flux patches (typically two at each hemisphere) that maintain the axial dipole are preferentially located below regions of high CMB heat flux (dashed red contours in Fig. 3). This configuration is disrupted during the reversal (see movie in SM); however, the magnetic field structures that dominate the transitional field are still concentrated in the high CMB heat flux longitudinal stripes below the Americas and east Asia. In Fig. 3b large positive mid-latitude magnetic flux patches below east Asia weaken the axial dipole, while in Fig. 3c small-scale magnetic flux patches below the Americas dominate the western hemisphere while the southern high latitudes are devoid of intense magnetic flux.

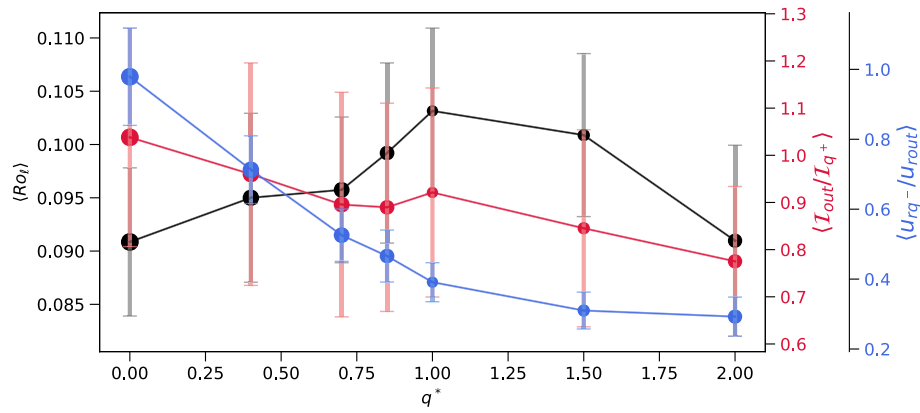


Figure 2. Diagnostics of the dynamo models vs. the outer boundary heat flux anomaly amplitude q^* . The local Rossby number Ro_l (13) is in black. The size of the symbols is proportional to the dipolarity f_{dip} (15). The ratio between the RMS azimuthal component of the inertial force at $r/r_o = 0.95$ outside/inside regions where $\delta q > \frac{1}{2}\delta q_{max}$ (17–18) is in red. The ratio between the RMS radial velocity at $r/r_o = 0.95$ inside/outside regions where $\delta q < \frac{1}{2}\delta q_{min}$ (19–20) is in blue. Error bars denote temporal variability.

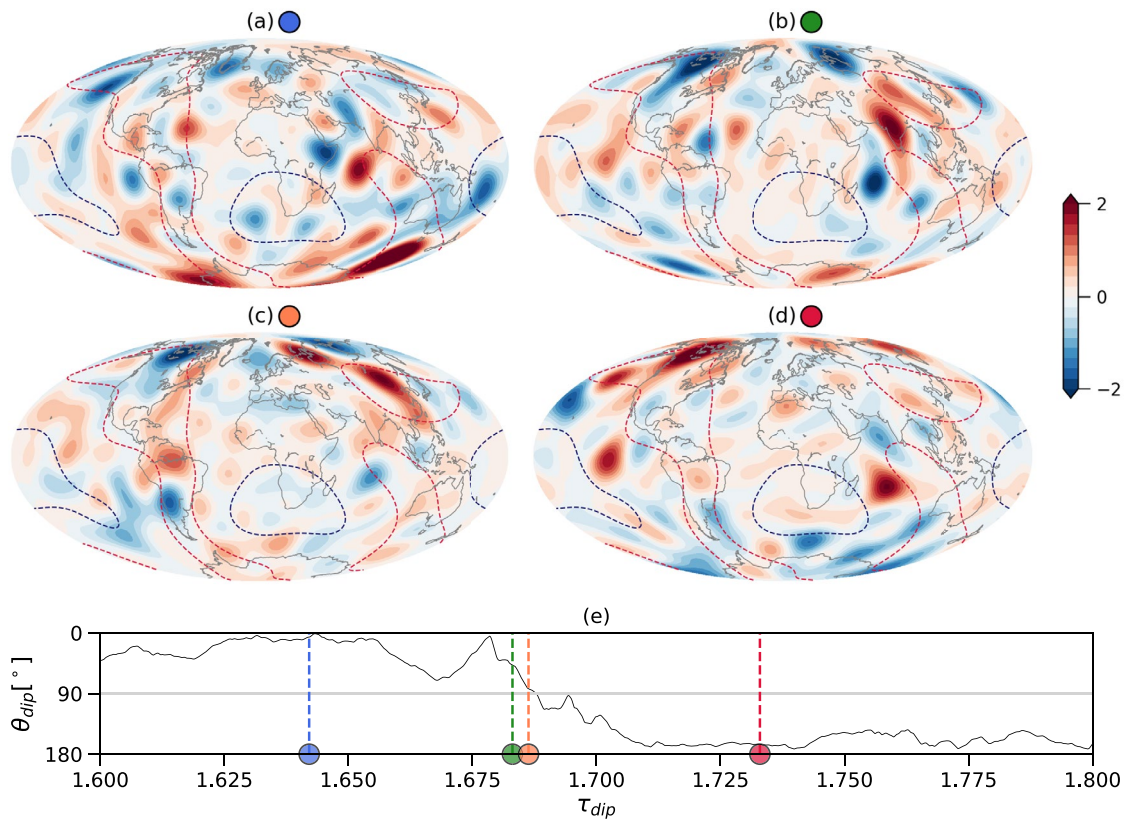


Figure 3. Snapshots of a simulated reversal. Non-dimensional radial magnetic field on the outer boundary of the dynamo model with $q^* = 1.5$ truncated at spherical harmonic degree and order 14. Dashed red and blue contours denote half maximum and half minimum of the imposed outer boundary heat flux anomaly respectively. The maps show the radial field before (a), during (b,c) and after (d) the reversal. The distance of the dipole axis from the north geographic pole vs. time in units of dipole diffusion times with the corresponding times for the four snapshots denoted by dashed vertical lines is given in (e).

For stronger mantle control ($q^* > 1$), the effect of increasing q^* is related to other CMB features. In these dynamo models, increasing q^* leads to more extensive regional subadiabatic conditions^{19,20} below Large Low Shear wave Velocity Provinces (LLSVPs; blue dashed contours in Fig. SM1, blue in Fig. 2). In these regions convection is suppressed and skin effects diffuse effectively small-scale magnetic fields²⁹ hence the dipole becomes relatively stronger and the likelihood for a reversal decreases. The distribution of radial velocity at the top of

the shell (Fig. 4) illustrates the emergence of regional subadiabatic conditions when the amplitude of the outer boundary heat flux heterogeneity exceeds unity. In the homogeneous case (Fig. 4a) convective cells extend until the outer boundary sporadically over the entire globe. When $q^* = 1$ (Fig. 4b) these convective structures are nearly absent from the regions below LLSVPs (see dashed contours), and even less radial flows reach the outer boundary in these regions for the dynamo model with $q^* = 2$ (Fig. 4c).

Discussion

We showed that an increase in the amplitude of the outer boundary heat flux heterogeneity within moderate values of $q^* < 1$ leads to a transition from non-reversing to reversing dynamos (Figs. 2 and SM4). In our dynamo models, reversals of the geomagnetic field are triggered below the Americas and east Asia where the CMB heat flux is anomalously large. Below these regions, relatively more heat is extracted from the core³⁰, leading to stronger convection and inertial effects (Fig. 1). Sahoo and Sreenivasan²² argued that enhanced turbulent conditions below regions of stronger CMB heat flux lead to fragmentation of the magnetic field structures. We propose that this regional fragmentation may eventually result in a global polarity reversal. While these regional inertial effects are strong enough to produce reversals, away from these large outer boundary heat flux regions inertial effects are secondary to the dominant first order ageostrophic Coriolis force, as expected for Earth's outer core^{7,11}. Upon further increase in the amplitude of outer boundary heat flux heterogeneity, the trend somewhat surprisingly changes, and the reversibility decreases (Figs. 2 and SM4). At $q^* > 1$ the heat flux becomes regionally subadiabatic below the African and Pacific LLSVPs^{19,20} and the convection there vanishes (Fig. 4), leading to skin effects that suppress small-scale contributions to the geomagnetic field²⁹ hence stabilize the dipole.

Somewhat various ranges were considered for the dipolarity f_{dip} that characterizes dipole-dominated dynamos (see³¹, and references therein). In addition, various values were reported for the critical local Rossby number that was proposed to mark the transition from dipole-dominated non-reversing (characterized by low Ro_ℓ) to multipolar reversing dynamos (characterized by large Ro_ℓ). This critical local Rossby number may depend on the convection style^{4,6,32}. In addition, the transition might not be sharp, i.e. some overlaps between these two dynamo regimes may prevail, which are of particular interest for recovering the behavior of the geomagnetic field over distinctive timescales. Menu et al.³³ reported non-reversing dynamos with large Ro_ℓ . Our dynamo models

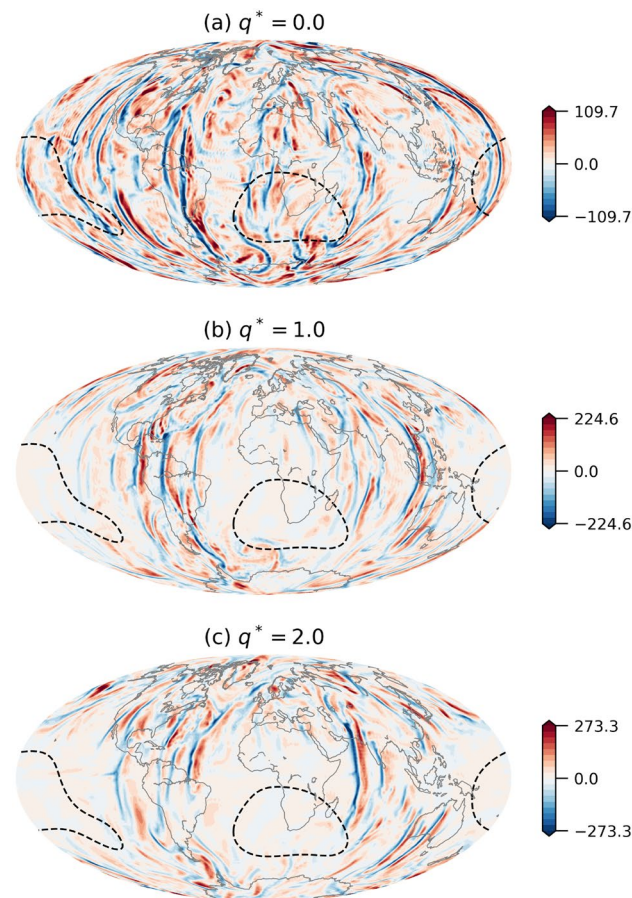


Figure 4. Non-dimensional radial velocity at the top of the shell ($r/r_o = 0.95$) for dynamo models with (a) $q^* = 0.0$, (b) $q^* = 1.0$ and (c) $q^* = 2.0$. Dashed contours denotes the regions where $\delta q < \frac{1}{2} \delta q_{min}$ (see Fig. SM1). Note the different scales.

highlight the impact of the boundary heterogeneity on the critical Ro_ℓ . Given a large enough amplitude of outer boundary heat flux heterogeneity, we found reversing dynamos with a relatively low Ro_ℓ of less than 0.1 (Fig. 2).

Our results of increasing reversibility for increasing q^* are in agreement with most previous studies (e.g.^{6,25}). In contrast, Mound and Davies³⁴ found that a reversing dynamo with homogeneous boundary conditions becomes non-reversing when q^* is increased. However, they introduced large leaps in q^* , possibly skipping the moderate q^* regime in which reversibility increases with q^* and reaching directly from homogeneous to the large q^* regime in which reversibility decreases with q^* (Fig. 2).

Stratification at the top of Earth's core may have emerged by various mechanisms, e.g. primordial origin³⁵, compositional convection³⁶, and more. Our finding that the reversibility decreases with q^* when it exceeds unity (Figs. 2 and SM4) is related to the impact of regional stratification on core dynamics and the geomagnetic field. Indeed, some results from seismology³⁷ and mineral physics³⁸ favor stable stratification at the top of the core, whereas inferences from the geomagnetic field³⁹ and its secular variation⁴⁰ provide evidence against a thick stable layer below the CMB. These contradicting results may be reconciled with partial stratification accommodated by CMB heat flux heterogeneity^{19,20}. Our dynamo models highlight a new dynamical aspect of partial stratification. According to our results, partial stratification driven by CMB heat flux heterogeneity (Fig. 4) may suppress regional small-scale contributions to the geomagnetic field which in turn leads to the stabilization of the dipole compared to cases with smaller q^* (Figs. 2 and SM4) and smaller CMB area under subadiabatic conditions.

Further increase beyond $q^* = 2$, which has not been explored in this study, might lead to failed dynamos. Olson and Christensen¹³ reported for models with two single harmonic outer boundary heat flux patterns (Y_2^2 and Y_2^0) that when $q^* > 1$ the dynamos fail. Likewise, for a particularly localized heat flux pattern (in the context of the past dynamo of Mars), above a critical heterogeneity amplitude cessation of the dynamos was found⁴¹. For a Y_1^0 pattern (again relevant to the past Martian dynamo), Yan et al.⁴² found that the dynamo failure depends on the convection style. Furthermore, the dynamo may resurrect for much larger q^* ⁴². Overall, in numerical dynamos with single harmonic outer boundary heat flux patterns the critical q^* value for dynamo failure may depend on the internal control parameters as well as the convection style (T. Frisson and N. Schaeffer, personal communication). Our study shows that when considering the multi harmonic tomographic CMB heat flux, self-consistent convection-driven dynamos are obtained until at least $q^* = 2$, in agreement with previous studies^{22,34}.

The results presented here may depend on our choice of convection style. The thermal and chemical buoyancy fluxes in the core are debated. Thermal convection depends on the total and adiabatic CMB heat fluxes, both of which are highly uncertain. In particular, the adiabatic heat flux depends on the thermal conductivity of the liquid core, a material property for which estimates are yet to converge (compare e.g.^{38,43}). Taking into account possible ranges for these CMB heat fluxes, both thermal superadiabatic and subadiabatic scenarios are possible⁴⁴. Chemical convection depends on the inner core growth rate, which is also uncertain. Cormier et al.⁴⁵ favor thermochemical core convection with dominant chemical convection, although different combinations of CMB total and adiabatic heat fluxes as well as inner core growth rate, all within their estimated ranges, may give anything from purely chemical convection to even dominant thermal convection! Here we naively set zero buoyancy sources/sinks, corresponding to thermochemical convection with equal thermal and chemical contributions. In a future study, it is worth testing the validity of our results for different partitionings of thermal and chemical buoyancy fluxes. Finally, a systematic parameter study is required to confirm our results for the dependence of the dynamo regime transitions on the amplitude of the CMB heat flux heterogeneity, both the transition from non-reversing to reversing dynamos as well as the transition from reversing to failed dynamos.

Methods

Numerical dynamo models

Numerical dynamo simulations are self-consistent solutions to the full set of magnetohydrodynamic (MHD) equations: conservation of momentum, electromagnetic induction, conservation of heat (or co-density), incompressibility and non-existent magnetic monopoles (e.g.⁴⁶). The Boussinesq approximation is applied, and gravity varies linearly with radial distance. These equations in non-dimensional form are respectively (e.g.^{46,47}):

$$E \left(\frac{\partial \mathbf{u}}{\partial t} + \mathbf{u} \cdot \nabla \mathbf{u} - \nabla^2 \mathbf{u} \right) + 2\hat{z} \times \mathbf{u} + \nabla P = Ra^* \frac{\mathbf{r}}{r_o} C + \frac{1}{Pm} (\nabla \times \mathbf{B}) \times \mathbf{B}, \quad (1)$$

$$\frac{\partial \mathbf{B}}{\partial t} = \nabla \times (\mathbf{u} \times \mathbf{B}) + \frac{1}{Pm} \nabla^2 \mathbf{B}, \quad (2)$$

$$\frac{\partial C}{\partial t} + \mathbf{u} \cdot \nabla C = \frac{1}{Pr} \nabla^2 C, \quad (3)$$

$$\nabla \cdot \mathbf{u} = 0, \quad (4)$$

$$\nabla \cdot \mathbf{B} = 0, \quad (5)$$

where \mathbf{u} is the fluid velocity, t time, \hat{z} the direction of the axis of rotation, P the pressure, \mathbf{r} the position vector, r_o the outer boundary radius, C the co-density and \mathbf{B} the magnetic field. The co-density is given by $C = \alpha T + \beta \xi$ where T is temperature, ξ light elements concentration and α and β their respective expansivities. Equations (1)–(3) contain four (internal) control parameters. The Ekman number represents the ratio of viscous to Coriolis forces:

$$E = \frac{\nu}{\Omega D^2}. \quad (6)$$

The heat flux based Rayleigh number represents the convection vigor vs. retarding forces:

$$Ra = \frac{\alpha g_0 q_0 D^4}{\kappa \nu k}. \quad (7)$$

The Prandtl number and the magnetic Prandtl number are ratios of diffusivities:

$$Pr = \frac{\nu}{\kappa}, \quad (8)$$

$$Pm = \frac{\nu}{\eta}. \quad (9)$$

Note that the modified Rayleigh number Ra^* in (1) is related to the classical Rayleigh number Ra in (7) by $Ra^* = RaE/Pr$. In (6)–(9) Ω is the rotation rate, ν the kinematic viscosity, D the shell thickness, g_0 the gravitational acceleration at the outer boundary, q_0 the mean outer boundary heat flux, k the thermal conductivity, κ the thermal diffusivity and η the magnetic diffusivity.

In all dynamo simulations we imposed rigid and electrically insulating conditions at both boundaries. The spherical shell has an Earth-like inner to outer core radii ratio of 0.35. No volumetric co-density source or sink was assigned, i.e. thermal buoyancy sources (primarily secular cooling) and chemical buoyancy sinks (light elements release from the freezing of the inner core) are assumed to balance each other, corresponding to thermochemical convection¹⁵. On the outer boundary of the simulations a heat flux pattern was imposed based on a tomographic model of seismic shear wave velocity anomalies at the lowermost mantle²⁸ truncated at spherical harmonic degree and order 6. The amplitude of the imposed heat flux heterogeneity is quantified by (e.g.¹³)

$$q^* = \frac{q_{max} - q_{min}}{2q_0}, \quad (10)$$

where q_{max} and q_{min} are the maximum and minimum heat flux respectively. For the inner boundary fixed co-density was imposed.

Several main outputs characterize the convection in the models. The magnetic Reynolds number, which measures the ratio of magnetic field advection to diffusion, is defined by

$$Rm = \frac{UD}{\eta} \quad (11)$$

where U is the rms velocity in the shell volume. In our dynamo models $Rm \sim 1500$ (Table SM1), somewhat larger yet on the same order of magnitude as the estimate for Earth's core (e.g.⁴⁸). The Rossby number is a conventional measure of the ratio of inertial to Coriolis forces:

$$Ro = \frac{U}{\Omega D}. \quad (12)$$

The local Rossby number⁴ accounts for the actual flow length-scale:

$$Ro_\ell = \frac{Ro \bar{\ell}_u}{\pi} \quad (13)$$

where ℓ_u is the characteristic wave-number of the flow obtained from the time-averaged kinetic energy spectrum:

$$\bar{\ell}_u = \frac{\sum \ell \langle \mathbf{u}_\ell \cdot \mathbf{u}_\ell \rangle}{2E_{kin}}. \quad (14)$$

Other outputs characterize the modeled magnetic fields, in particular the dipole. The relative dipole field strength on the outer boundary is defined by

$$f_{dip} = \left(\frac{\frac{4}{3} ((g_1^0)^2 + (g_1^1)^2 + (h_1^1)^2)}{\sum_{\ell=1}^{12} \sum_{m=0}^{\ell} \frac{(\ell+1)^2}{2\ell+1} ((g_\ell^m)^2 + (h_\ell^m)^2)} \right)^{1/2} \quad (15)$$

where ℓ and m are the spherical harmonics degree and order respectively. In addition we calculate the time-average dipole tilt. In the reversing dynamos we fold the tilt angle to the northern hemisphere so that the resulting quantity $\langle \theta_{dip} \rangle$ represents the average distance from the geographic pole ($\langle \rangle$ denotes time averaging). Because a model in which a reversal has not been observed is not guaranteed to be non-reversing, $\langle \theta_{dip} \rangle$ serves as a practical measure of reversibility for finite simulation times (which is always the case). In Table SM1 the $\langle \theta_{dip} \rangle$ values are given for all models. Note that in the non-reversing models ($q^* = 0 - 0.75$) $\langle \theta_{dip} \rangle$ is below 10° , whereas in the reversing models ($q^* = 0.85 - 2$) $\langle \theta_{dip} \rangle$ is $\sim 20^\circ$ and above.

In the dynamo models output, time is given in units of viscous diffusion times $\tau_\nu = D^2/\nu$. The magnetic diffusion time $\tau_\eta = D^2/\eta$ is simply related to the viscous diffusion time by $\tau_\eta = Pm\tau_\nu$. In the context of magnetic

field reversals, it is common practice to express the results in terms of the dipole diffusion time⁴⁹ $\tau_{dip} = \frac{r_o^2}{\pi^2 \eta}$. In terms of the viscous diffusion time,

$$\tau_{dip} = Pm \left(\frac{r_o}{\pi D} \right)^2 \tau_v. \quad (16)$$

For Earth's core $\tau_{dip} \sim 38$ kyrs.

Regional measures of boundary control

Heterogeneous boundary control on the convection in the shell and the resulting magnetic field are quantified by focusing on specific regions at the top of the shell. Large outer boundary heat flux regions are defined by a heat flux anomaly larger than half the maximum, i.e. $\delta q > \frac{1}{2} \delta q_{max}$. To quantify regional triggering of reversals (relevant for moderate $q^* < 1$), we measure the time-average ratio between the RMS of the azimuthal component of the inertial force at $r/r_o = 0.95$ outside/inside regions where $\delta q > \frac{1}{2} \delta q_{max}$ which we denote as $\langle I_{out}/I_{q^+} \rangle$, with

$$\langle I_{q^+} \rangle = \left\langle \sqrt{\frac{\int_{q^+} I_{\phi}^2 dS}{\int_{q^+} dS}} \right\rangle \quad (17)$$

$$\langle I_{q_{out}} \rangle = \left\langle \sqrt{\frac{\int_{q_{out}} I_{\phi}^2 dS}{\int_{q_{out}} dS}} \right\rangle \quad (18)$$

where the surface increment is $dS = r^2 \sin \theta d\phi d\theta$. The integrations in (17) are over the large heat flux regions where $\delta q > \frac{1}{2} \delta q_{max}$, whereas the integrations in (18) are over the remaining CMB surface.

In contrast, to quantify regional suppression of reversals (relevant for larger $q^* > 1$), we measure the time-average ratio between the RMS radial velocity at $r/r_o = 0.95$ inside/outside regions where $\delta q < \frac{1}{2} \delta q_{min}$ which we denote as $\langle u_{rq^-}/u_{rout} \rangle$, with

$$\langle u_{rq^-} \rangle = \left\langle \sqrt{\frac{\int_{q^-} u_r^2 dS}{\int_{q^-} dS}} \right\rangle \quad (19)$$

$$\langle u_{rq_{out}} \rangle = \left\langle \sqrt{\frac{\int_{q_{out}} u_r^2 dS}{\int_{q_{out}} dS}} \right\rangle \quad (20)$$

The integrations in (19) are over the low heat flux regions where $\delta q < \frac{1}{2} \delta q_{min}$, while the integrations in (20) are over the remaining CMB surface.

Data availability

Data will be provided upon request.

Received: 30 December 2023; Accepted: 16 April 2024

Published online: 26 April 2024

References

- Glatzmaier, G. A. & Roberts, P. H. A three-dimensional self-consistent computer simulation of a geomagnetic field reversal. *Nature* **377**, 203–209 (1995).
- Aubert, J., Aurnou, J. & Wicht, J. The magnetic structure of convection-driven numerical dynamos. *Geophys. J. Int.* **172**, 945–956 (2008).
- Christensen, U. R. & Aubert, J. Scaling properties of convection-driven dynamos in rotating spherical shells and application to planetary magnetic fields. *Geophys. J. Int.* **166**, 97–114 (2006).
- Olson, P. & Christensen, U. R. Dipole moment scaling for convection-driven planetary dynamos. *Earth Planet. Sci. Lett.* **250**, 561–571 (2006).
- Driscoll, P. & Olson, P. Polarity reversals in geodynamo models with core evolution. *Earth Planet. Sci. Lett.* **282**, 24–33 (2009).
- Olson, P. & Amit, H. Magnetic reversal frequency scaling in dynamos with thermochemical convection. *Phys. Earth Planet. Inter.* **229**, 122–133 (2014).
- Yadav, R. K., Gastine, T., Christensen, U. R., Wolk, S. J. & Poppenhaeger, K. Approaching a realistic force balance in geodynamo simulations. *Proc. Nat. Sci. Acad. USA* **113**, 12065–12070 (2016).
- Aubert, J., Gastine, T. & Fournier, A. Spherical convective dynamos in the rapidly rotating asymptotic regime. *J. Fluid. Mech.* **813**, 558–593 (2017).
- Schaeffer, N., Jault, D., Nataf, H.-C. & Fournier, A. Turbulent geodynamo simulations: A leap towards Earth's core. *Geophys. J. Int.* **189**, 1–29 (2017).
- Aubert, J. Approaching Earth's core conditions in high resolution geodynamo simulations. *Geophys. J. Int.* **219**(S1), S137–S151 (2019).
- Schwaiger, T., Gastine, T. & Aubert, J. Force balance in numerical geodynamo simulations: A systematic study. *Geophys. J. Int.* **51**, S101–S114 (2019).
- Long, R. S., Mound, J. R., Davies, C. J. & Tobias, S. M. Scaling behaviour in spherical shell rotating convection with fixed-flux thermal boundary conditions. *J. Fluid Mech.* **889**, 690–732 (2020).

13. Olson, P. & Christensen, U. R. The time averaged magnetic field in numerical dynamos with nonuniform boundary heat flow. *Geophys. J. Int.* **151**, 809–823 (2002).
14. Gubbins, D., Willis, P. W. & Sreenivasan, B. Correlation of Earth's magnetic field with lower mantle thermal and seismic structure. *Phys. Earth Planet. Inter.* **162**, 256–260 (2007).
15. Aubert, J., Amit, H., Hulot, G. & Olson, P. Thermo-chemical wind flows couple Earth's inner core growth to mantle heterogeneity. *Nature* **454**, 758–761 (2008).
16. Amit, H., Aubert, J. & Hulot, G. Stationary, oscillating or drifting mantle-driven geomagnetic flux patches?. *J. Geophys. Res.* **115**, B07108. <https://doi.org/10.1029/2009JB006542> (2010).
17. Aubert, J., Finlay, C. C. & Fournier, F. Bottom-up control of geomagnetic secular variation by the Earth's inner core. *Nature* **502**, 219–223 (2013).
18. Amit, H. *et al.* Towards more realistic core-mantle boundary heat flux patterns: A source of diversity in planetary dynamos. *Prog. Earth Planet. Sci.* **2**, 26. <https://doi.org/10.1186/s40645-015-0056-3> (2015).
19. Olson, P., Landeau, M. & Reynolds, E. Dynamo tests for stratification below the core-mantle boundary. *Phys. Earth Planet. Inter.* **271**, 1–18 (2017).
20. Mound, J., Davies, C., Rost, S. & Aurnou, J. Regional stratification at the top of earth's core due to core-mantle boundary heat flux variations. *Nat. Geosci.* **12**, 575–580 (2019).
21. Terra-Nova, F., Amit, H. & Choblet, G. Preferred locations of weak surface field in numerical dynamos with heterogeneous core-mantle boundary heat flux: Consequences for the South Atlantic Anomaly. *Geophys. J. Int.* **217**(2), 1179–1199 (2019).
22. Sahoo, S. & Sreenivasan, B. Response of Earth's magnetic field to large lower mantle heterogeneity. *Earth Planet. Sci. Lett.* **549**, 116507 (2020).
23. Lézin, M., Amit, H., Terra-Nova, F. & Wardinski, I. Mantle-driven north-south dichotomy in geomagnetic polar minima. *Phys. Earth Planet. Inter.* **337**, 107000 (2023).
24. Glatzmaier, G., Coe, R., Hongre, L. & Roberts, P. The role of the earth's mantle in controlling the frequency of geomagnetic reversals. *Nature* **401**, 885–890 (1999).
25. Olson, P. L., Coe, R. S., Driscoll, P. E., Glatzmaier, G. A. & Roberts, P. H. Geodynamo reversal frequency and heterogeneous core-mantle boundary heat flow. *Phys. Earth Planet. Inter.* **180**, 66–79 (2010).
26. Heimpel, M. H. & Evans, M. E. Testing the geomagnetic dipole and reversing dynamo models over Earth's cooling history. *Phys. Earth Planet. Inter.* **224**, 124–131 (2013).
27. Amit, H. & Olson, P. Lower mantle superplume growth excites geomagnetic reversals. *Earth Planet. Sci. Lett.* **414**, 68–76 (2015).
28. Masters, G., Laske, G., Bolton, H. & Dziewonski, A. The relative behavior of shear velocity, bulk sound velocity, and compressional velocity in the mantle: Implications for chemical and thermal structure. In *Earth's Deep Interior: Mineral Physics and Tomography From the Atomic to the Global Scale* Vol. 117 (eds Karato, S. *et al.*) (AGU monograph, 2000).
29. Christensen, U. A deep dynamo generating Mercury's magnetic field. *Nature* **444**, 1056–1058 (2006).
30. Gubbins, D. Thermal core-mantle interactions: Theory and observations. In *Earth's Core: Dynamics, Structure and Rotation* (eds Dehant, V. *et al.*) (AGU Geodynamics Series - American Geophysical Union, 2003).
31. Davies, C. J. *et al.* Dynamo constraints on the long-term evolution of Earth's magnetic field strength. *Geophys. J. Int.* **228**, 316–336 (2021).
32. Wicht, J., Stellmach, S. & Harder, H. Numerical models of the geodynamo: From fundamental Cartesian models to 3D simulations of field reversals. In *Geomagnetic Field Variations - Space-Time Structure, Processes, and Effects on System Earth* (eds Glassmeier, H. *et al.*) (Springer, 2009).
33. Menu, M. D., Petitdemange, L. & Galtier, S. Magnetic effects on fields morphologies and reversals in geodynamo simulations. *Phys. Earth Planet. Inter.* **307**, 106542 (2020).
34. Mound, J. E. & Davies, C. J. Longitudinal structure of Earth's magnetic field controlled by lower mantle heat flow. *Nat. Geosci.* **16**, 380–385 (2023).
35. Bouffard, M., Landeau, M. & Goument, A. Convective erosion of a primordial stratification atop Earth's core. *Geophys. Res. Lett.* **47**, e2020GL087109 (2020).
36. Bouffard, M., Choblet, G., Labrosse, S. & Wicht, J. Chemical convection and stratification in the Earth's outer core. *Front. Earth Sci.* **7**, 99 (2019).
37. Kaneshima, S. Array analyses of SmKS waves and the stratification of Earth's outermost core. *Phys. Earth Planet. Inter.* **276**, 234–246 (2018).
38. Pozzo, M., Davies, C., Gubbins, D. & Alfè, D. Thermal and electrical conductivity of iron at Earth's core conditions. *Nature* **485**, 355–358 (2012).
39. Gastine, T., Aubert, J. & Fournier, A. Dynamo-based limit to the extent of a stable layer atop Earth's core. *Geophys. J. Int.* **1433–1448**, 222 (2020).
40. Amit, H. Can downwelling at the top of the Earth's core be detected in the geomagnetic secular variation?. *Phys. Earth Planet. Inter.* **229**, 110–121 (2014).
41. Sreenivasan, B. & Jellinek, A. M. Did the Tharsis plume terminate the Martian dynamo?. *Earth Planet. Sci. Lett.* **349–350**, 209–217 (2012).
42. Yan, C. *et al.* An ancient Martian dynamo driven by hemispheric heating: Effect of thermal boundary conditions. *Planet. Sci. J.* **4**, 11 (2023).
43. Konôpková, Z., McWilliams, R., Gómez-Pérez, N. & Goncharov, A. F. Direct measurement of thermal conductivity in solid iron at planetary core conditions. *Nature* **534**, 99–101 (2016).
44. Davies, C. & Greenwood, S. Dynamics in Earth's core arising from thermo-chemical interactions with the mantle. In *Core-Mantle Coevolution: A Multidisciplinary Approach. Geophysical Monograph Series* (eds Nakagawa, T. *et al.*) 219–258 (American Geophysical Union, 2003).
45. Cormier, V., Bergman, M. & Olson, P. *Earth's Core: Geophysics of a Planet's Deepest Interior* (Elsevier, 2021).
46. Olson, P., Christensen, U. R. & Glatzmaier, G. A. Numerical modeling of the geodynamo: Mechanisms of field generation and equilibration. *J. Geophys. Res.* **104**, 10383–110404 (1999).
47. Wicht, J. Inner-core conductivity in numerical dynamo simulations. *Phys. Earth Planet. Inter.* **132**, 281–302 (2002).
48. Christensen, U. R., Aubert, J. & Hulot, G. Conditions for Earth-like geodynamo models. *Earth Planet. Sci. Lett.* **296**, 487–496 (2010).
49. Moffatt, H. *Magnetic Field Generation in Electrically Conducting Fluids* (Cambridge University Press, 1978).

Acknowledgements

We acknowledge the financial support from the French Agence Nationale de Recherche, project DYRE-COMB (grant ANR-22-CE49-0016-01). F.T.-N. was supported by the Centre national d'études spatiales (CNES). We thank two anonymous reviewers for their constructive comments. We thank Thomas Gastine and Guy Moebs for their help with the Magic dynamo code (<https://github.com/magic-sph/magic>). Numerical dynamo simulations were performed on the GLICID (le Groupement Ligérien pour le Calcul Intensif Distribu ) computational center.

Author contributions

Both authors equally contributed to the manuscript.

Competing interests

The authors declare no competing interests.

Additional information

Supplementary Information The online version contains supplementary material available at <https://doi.org/10.1038/s41598-024-59849-z>.

Correspondence and requests for materials should be addressed to F.T.-N.

Reprints and permissions information is available at www.nature.com/reprints.

Publisher's note Springer Nature remains neutral with regard to jurisdictional claims in published maps and institutional affiliations.



Open Access This article is licensed under a Creative Commons Attribution 4.0 International License, which permits use, sharing, adaptation, distribution and reproduction in any medium or format, as long as you give appropriate credit to the original author(s) and the source, provide a link to the Creative Commons licence, and indicate if changes were made. The images or other third party material in this article are included in the article's Creative Commons licence, unless indicated otherwise in a credit line to the material. If material is not included in the article's Creative Commons licence and your intended use is not permitted by statutory regulation or exceeds the permitted use, you will need to obtain permission directly from the copyright holder. To view a copy of this licence, visit <http://creativecommons.org/licenses/by/4.0/>.

© The Author(s) 2024